Ionics (2024) 30:3403–3416
https://doi.org/10.1007/s11581-024-05532-2

RESEARCH

Preparation of high-entropy alloy bifunctional catalysts with rare earth Ce coordination and Efficient water splitting research

Zhang Wenyu[1,2,3] · Guo Ruihua[1,2] · Yue QuanXin[1,2,3] · Huang Yarong[1] · Zhang GuoFang[1] · Guan LiLi[1,2]

Received: 1 March 2024 / Revised: 5 April 2024 / Accepted: 11 April 2024 / Published online: 17 April 2024

Abstract

In the electrolytic water hydrogen production, the slow electrocatalytic kinetics of the hydrogen evolution reaction (HER) and oxygen evolution reaction (OER) limit the energy conversion efficiency. Multi-metal high-entropy alloys (HEAs) are considered potential catalysts to replace traditional metal oxides and precious metals in energy conversion and water electrolysis. In this study, a solution of Fe, Co, Ni, Mo, and Ce halide salts was formed through hydrogen bonding with a chelating agent, citric acid (CA). After thermolysis, a highly efficient and stable rare earth (RE) Ce-coordinated single-phase non-precious metal high-entropy alloy (HEA) was obtained. Under alkaline conditions for the oxygen evolution reaction (OER), the overpotential of FeCoNiMoCe HEA/C was only 260 mV at a current density of 10 mA cm^{-2}, which is 40 mV lower than that of commercial RuO_2. Under alkaline conditions for the hydrogen evolution reaction (HER), FeCoNiMoCe HEA/C had an overpotential of only 130 mV at a current density of 10 mA cm^{-2}, which is only 60 mV higher than that of commercial Pt/C catalyst. The FeCoNiMoCe HEA/C displayed excellent catalytic activity in the overall water splitting system. This is due to the atomic disorder of high-entropy alloy catalysts, which provides more reaction sites, thereby increasing reaction activity and selectivity. Our work presents a straightforward and feasible synthetic strategy for preparing high-entropy compounds, which holds great potential in energy and electrocatalysis applications through entropy engineering.

Keywords High-entropy alloy · Rare earth elements · Bifunctional catalyst · Overall water splitting

Introduction

The use of fossil fuels has led to energy crises and greenhouse effects. Developing a clean, sustainable energy source to replace traditional fossil fuels is crucial in mitigating severe environmental issues and the global energy crisis [1–4]. Hydrogen energy is a green renewable energy that can replace fossil fuels and has broad research prospects. Hydrogen energy has a significantly higher energy density and combustion heat value compared to other fuels [5, 6]. Electrolysis of water to produce hydrogen is widely regarded as one of the most promising technologies for achieving carbon neutrality through hydrogen fuel production [7–10]. However, the efficiency of water electrolysis is significantly affected by the limitations of high-performance catalysts for the oxygen-evolution reaction (OER) and hydrogen-evolution reaction (HER). This hinders the industrial-scale electrolysis of water [11–19]. The efficiency of water electrolysis depends heavily on the catalyst used. Only by using excellent electrocatalysts can efficient hydrogen production be achieved. Precious metal catalysts such as Pt/C and RuO_2 have traditionally been recognized as benchmark HER and OER catalysts and have been commercially applied in water splitting [20]. However, the practical applications of these resources are hindered by their high cost and natural scarcity [21–23]. Thus, there is an urgent need to develop non-precious metal materials to enhance the overall efficiency of water electrolysis.

The catalytic activity of single metal or bimetallic catalysts depends largely on the adsorption of reactants on the

✉ Guo Ruihua
grh7810@163.com

1 School of Material and Metallurgy, Inner Mongolia University of Science & Technology, Baotou 014010, China

2 Inner Mongolia Key Laboratory of Advanced Ceramic Materials and Devices, Inner Mongolia University of Science & Technology, Baotou 014010, China

3 Key Laboratory of Green Extraction & Efficient Utilization of Light Rare-Earth Resources, Ministry of Education, Inner Mongolia University of Science & Technology, Baotou 014010, China

active sites of their surfaces [24–26]. However, achieving optimal binding energy for all intermediates on the limited number of active sites available simultaneously is not possible [27, 28]. To overcome this limitation, scientists have devoted themselves to developing novel multimetal catalysts. Multimetal catalysts have a greater number of active sites, enabling the simultaneous adsorption and catalysis of multiple intermediates. This leads to an improvement in the efficiency and selectivity of the reaction. By rationally designing the composition and structure of the catalyst, synergistic effects between intermediates at different active sites can be achieved, further enhancing the catalytic performance. High-entropy alloys (HEAs) are alloys that contain at least five specific elements, with each element having an atomic concentration ratio between 5 and 35% [29–31]. HEAs have a strong lattice due to the combination of various catalytically active elements with different atomic sizes. This leads to lower energy barriers for catalytic reactions, unlike transition metal-based electrocatalysts [32], Electrocatalysts known as HEAs have garnered significant attention due to their unique chemical and physical properties. These properties include diverse element selection, high chemical and thermal stability, multiple active sites, and high configurational entropy [33–35].

Transition metals are typical representatives of high-activity, low-cost electrocatalysts with rich d-electrons, which are crucial for electron transfer and participation in chemical reactions [36]. The d-electrons participate in charge transfer and electron transfer processes, thereby promoting electrocatalytic reactions. Additionally, the diverse distribution of d-electron energy levels in transition metals allows for the adjustment of catalytic activity and selectivity by controlling the electron energy levels. Transition metals provide suitable energy levels and vacancies, facilitate electron transfer and participation in catalytic reactions, thereby accelerating reaction rates and reducing overpotential and energy losses in electrocatalysis [37, 38]. Furthermore, the unique filling states and strong electron supply capability of Mo 4d orbitals can regulate the electron structure of catalysts, changing their band structure and electron distribution, thereby affecting the catalytic activity of the catalyst. The introduction of Mo can introduce additional d-electrons, increasing the electron density of the catalyst and enhancing the interaction between the catalyst and the reactants, facilitating the adsorption of the reactants and the reaction processes [39]. The integration or doping of transition metal-based electrocatalysts with rare earth elements began in the 1970s with $LaNi_5$ and has developed rapidly in the twenty-first century, with non-noble metals such as Co, Ni, and Fe being combined with rare earth (RE) elements for use in electrocatalytic reactions. In particular, Ce and its oxides have attracted particular interest in electrocatalytic reactions due to their rapid transfer between the Ce^{3+}/Ce^{4+} redox couple. According to the Brewer-Engel theory, alloying metals from the left half of the transition metal sequence in the periodic table (i.e., metals with empty or less filled d orbitals) with metals from the right half of the sequence (i.e., metals with more filled d bands) leads to the maximum bonding strength and stability of the metal alloy, resulting in significant synergistic effects [40]. Currently, research on high-entropy alloys primarily focuses on the selection of precious and common transition metals. Rare earth elements are effectively added to the catalyst system to optimize the charge distribution at the interface due to the difference in electronegativity between rare earth and common transition metals. This optimization results in unique electronic and catalytic properties in rare earth-containing alloy catalysts [41]. This is due to the effective shielding of electrons in the 4f subshell by electrons in the outer 5 s and 5p subshells [42]. Rare earth elements can be used to control the electronic structure of active sites in alloys, allowing for the design of new catalyst materials [43, 44].

Currently, compared with electrocatalysts below ternary, high-entropy alloys have a rich component modulation range and a complex surface interface structure, providing the possibility of achieving a nearly continuous distribution of adsorption energy curves [45, 46]. However, the synthesis strategy of high-entropy alloys (HEAs) still faces challenges due to the difficulty of mixing different elements and avoiding aggregation and migration phenomena. In recent years, high-energy ball milling and solid-state alloying have been simple methods for large-scale production of HEAs, but they cannot control the size and morphology of HEAs [47–49]. Methods such as carbothermal shock, laser melting, and arc melting can rapidly produce the desired HEA, but the HEA produced at extremely high temperatures limits its large-scale production [50, 51]. Recently, the wet impregnation method has been considered the most popular method for the preparation of HEA because it has the advantages of low operational difficulty and high controllability, making it suitable for large-scale production [52, 53]. However, the use of multi-ligand materials such as 1,10-phenanthroline and poly(N-vinyl-2-pyrrolidone) for the aggregation of metal precursors is environmentally toxic and harmful [54, 55]. Here, we have developed a novel and convenient critical acid polymerization strategy using citric acid (CA) as a natural material and combining it with halide salts to form hydrogen bonding networks [33, 56]. Following a pyrolysis process, we directly synthesize high-entropy alloys of Fe, Co, Ni, Mo, and rare earth Ce (FeCoNiMoCe HEA/C) using this method. Both three-metal FeCoNi/C and four-metal FeCoNiMo/C can be synthesized with the same phase structure, demonstrating the universality of this preparation strategy. As expected, the obtained alloys show continuously improved performance in terms of OER, HER, and overall water splitting with an increasing number of metal

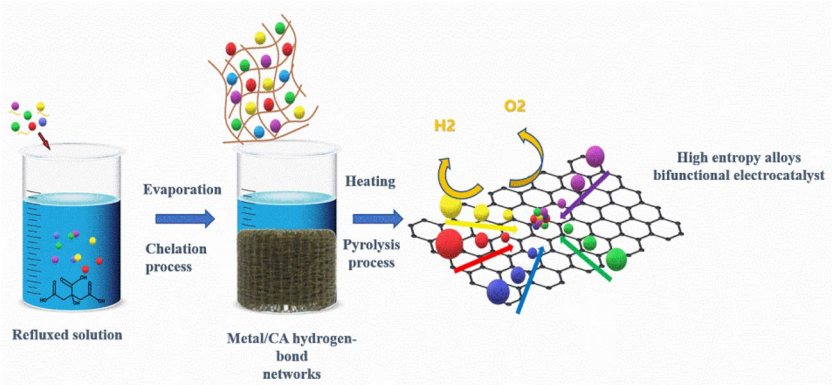

Scheme 1 Schematic diagram of the reaction of FeCoNiMoCe HEA/C

types. In particular, FeCoNiMoCe HEA/C as bifunctional electrocatalysts show the best activity in a 1 mol KOH solution at 10 mA cm^{-2} with overpotentials of 260 and 130 mV. Using FeCoNiMoCe HEA/C as both electrode materials, an integrated electrolyzer requires a voltage of only 1.6 V to achieve a current density of 10 mA cm^{-2}. The positive correlation between the number of metal types and electrocatalytic performance highlights the importance of synthesizing of new HEAs and their immense potential for catalytic applications.

Experiment section

Ferric chloride ($FeCl_3$-$6H_2O$), nickel chloride ($NiCl_2$-$6H_2O$), cobalt chloride ($CoCl_2$-$6H_2O$), molybdenum chloride ($MoCl_5$), cerium chloride ($CeCl_3$), citric acid ($C_6H_8O_7$-H_2O), and potassium hydroxide (KOH) were purchased from Shanghai Maclyn Biochemical Technology Co., Ltd. RuO_2 was purchased from Suzhou Senno Technology Co., Ltd. Pt/C was purchased from Shanghai Kesen Electric Co., Ltd. Ar gas was obtained from Inner Mongolia Zhongkebiaowu Technology Co., Ltd. Deionized water was used in the experiment. All reagents were used as received without any further purification.

In a typical synthesis, equimolar amounts of metal precursors ($FeCl_3$-$6H_2O$, $CoCl_2$-$6H_2O$, $NiCl_2$-$6H_2O$, $MoCl_5$, $CeCl_3$) were dissolved in a 30 mL ethanol–water solution saturated with argon. The mixture was then stirred for 60 min. Next, 8 mmol of citric acid ($C_6H_8O_7$-H_2O) was added to the solution, and after 30 min of stirring, the resulting solution is refluxed at 90℃ for 2 h to form a sol. The gel ash resulting from the evaporation of the mixture at 120℃ for 10 h is collected and ground. The ground gel ash is then heated under argon conditions at a rate of 5℃ min^{-1} to 200℃ and held for 2 h, followed by heating at a rate of 10℃ min^{-1} to 800℃ for 3 h, resulting in black powder.

The synthesis procedure for FeCoNiMo/C and FeCoNi/C is the same as that for FeCoNiMoCe HEA/C, with the addition of respective metal sources. The amount of citric acid used is 6 mmol and 4.5 mmol, respectively.

Results and discussions

Scheme 1 illustrates the preparation process and reaction principle of FeCoNiMoCe HEA/C. In this study, citric acid ($C_6H_8O_7$, CA) is chosen as a complexing agent, which contains numerous -COOH and -OH groups capable of chelating halide salts to form a homogeneous multi-metal sol network. After refluxing and evaporating, CA polymerizes with metal chlorides and forms a uniform network through hydrogen bonding [57, 58], effectively preventing the aggregation of metal chlorides. The synthesis mechanism is driven by the decomposition of metal salts and the release of CO gas [51]:

$$MCl_xH_y \rightarrow M + gases \uparrow \quad (1)$$

$$C + O^* \rightarrow CO \uparrow \quad (2)$$

O* refers to residual oxygen that is surface-bound. During the pyrolysis process, carbon metabolism reactions can occur, involving carbon (fuel), metals (catalysts), and O* (oxidants). Mechanistically, metals with catalytic sites can accelerate intense carbon metabolism reactions, leading to higher frequency of metal movement [51]. This process can result in the formation of uniformly dispersed high-entropy alloys.

To investigate the hybrid graphite structure and structural defects of FeCoNiMoCe HEA/C, FeCoNiMo/C, and FeCoNi/C catalysts, Raman spectroscopy was employed to analyze the obtained catalysts. As shown in Fig. S2, the Raman spectrum of the samples shows two prominent peaks at 1340 cm^{-1} (D band, associated with structural defects or disordered carbon atoms) and 1579 cm^{-1} (G band, corresponding to graphitic carbon atoms). The degree of graphitization and structural defects in the materials is typically indicated by the intensity ratio of the D band to the G band

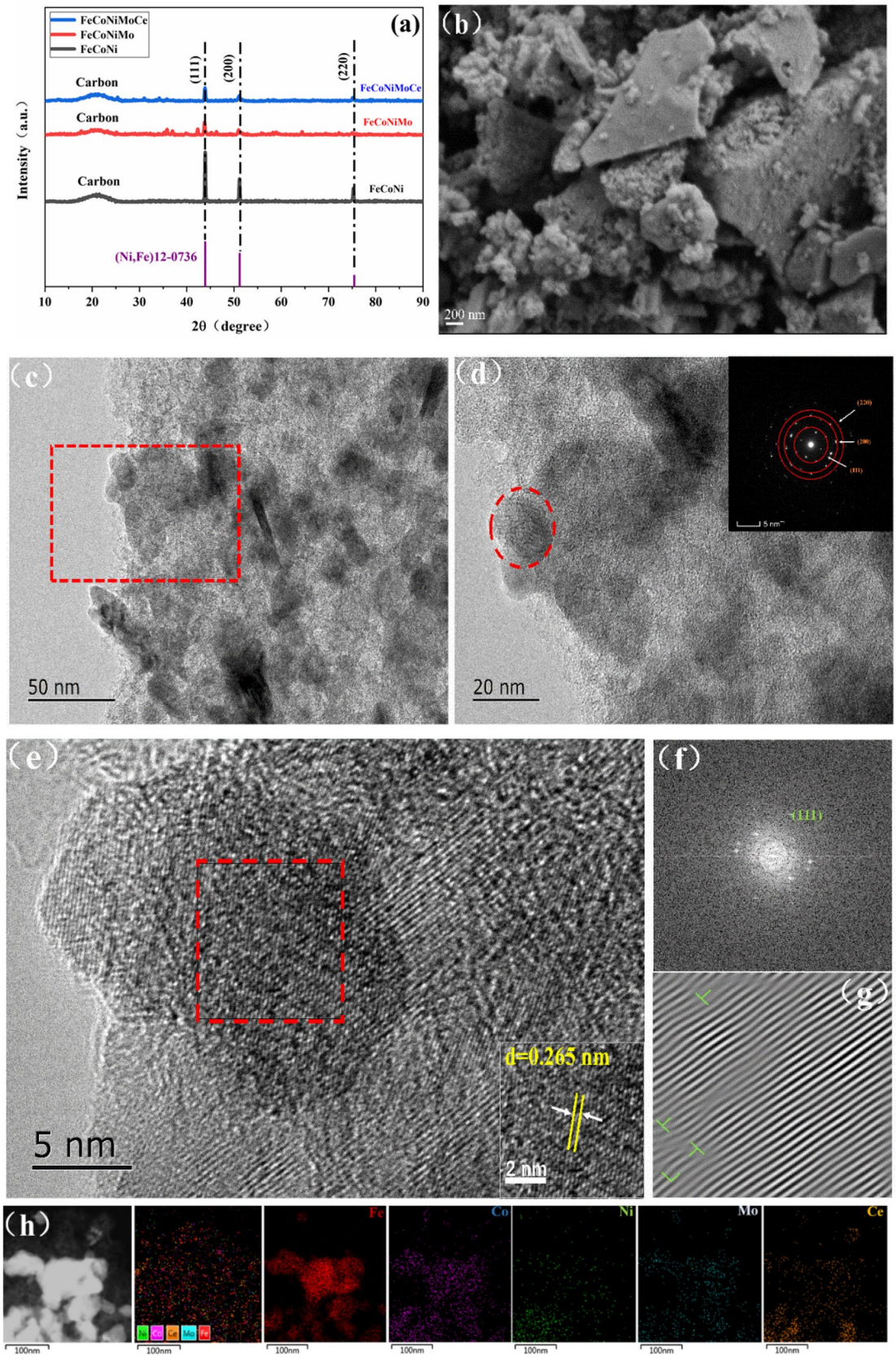
(a)
FeCoNiMoCe
FeCoNiMo
FeCoNi
(111)
(200)
(220)
Carbon
Carbon
Carbon
FeCoNiMoCe
FeCoNiMo
FeCoNi
(Ni,Fe)12-0736
Intensity (a.u.)
10 20 30 40 50 60 70 80 90
2θ (degree)
(b)
200 nm
(c)
50 nm
(d)
(220)
(200)
(111)
5 nm⁻¹
20 nm
(e)
5 nm
d=0.265 nm
2 nm
(f)
(111)
(g)
(h)
Fe
Co
Ni
Mo
Ce
100nm

◂**Fig. 1** **a** XRD patterns of FeCoNi/C, FeCoNiMo/C, and FeCoNiMoCe HEA/C; **b** SEM images of the synthesized FeCoNiMoCe HEA/C; **c** TEM image of FeCoNiMoCe HEA/C; **d** HRTEM image of the magnified TEM image from the red square region in c. Corresponding SAED pattern is shown as inset; **e** HRTEM image of the particles in the red region; **f** FFT image obtained from the red region; **g** lattice planes of the particles in the red region; **h** elemental mapping of FeCoNiMoCe HEA/C

(I_D/I_G), with a standard value of 1.0. The calculated I_D/I_G values were about 1.03, 0.87, and 0.83, respectively. Among them, the FeCoNiMoCe/C catalyst has the highest intensity ratio, indicating the presence of the most carbon structural defects, which are beneficial for providing excellent reaction sites for the reaction.

As shown in Fig. 1a, the X-ray diffraction (XRD) patterns of FeCoNi/C, FeCoNiMo/C, and FeCoNiMoCe HEA/C samples exhibit a single-phase face-centered cubic (fcc) structure. The peaks located at 42.9°, 50.2°, and 74.6° correspond to the (111), (200), and (220) crystal planes, respectively. In addition, for FeCoNiMo/C, we have also observed additional peaks corresponding to Fe_2Mo3O_8#74–1429, as shown in Figure S2a. This can be attributed to partial oxidation that may have occurred during the storage and testing of FeCoNiMo/C. Similarly, we have observed this phenomenon in FeCoNiMoCe HEA/C as well (Figure S2b). However, compared to FeCoNiMo/C, the intensity of the peaks corresponding to other phases in FeCoNiMoCe HEA/C is significantly lower, indicating the high-entropy effect of high-entropy alloys (increased configurational entropy with an increasing number of elements, leading to a reduction of the correlated free energy at high temperatures and the formation of a single-phase structure) [49]. In particular, the diffraction peak positions of FeCoNiMoCe HEA/C samples are significantly shifted to the left compared to the diffraction peaks of FeCoNi/C. This indicates that, according to the Bragg equation, the addition of large Ce atoms increases the lattice spacing, resulting in a decrease in the diffraction angle θ (as shown in Fig. S3). This suggests that these elements have been successfully incorporated into the nanocatalyst to form the HEA structure. Additionally, the chemical composition analysis of the HEA was performed using inductively coupled plasma optical emission spectroscopy (ICP-OES), and the results are shown in Table S1, Ni:Fe:Co:Mo:Ce = 1:0.99:0.96:0.89:0.85, with each metal content ranging from 5–35 at.%, consistent with the definition of high entropy alloys [35].

As shown in Fig. S4(a)(b), FeCoNiMoCe HEA/C has a powdery shape with rough surface. The TEM image in Fig. S5 shows that FeCoNiMoCe HEA/C has a uniform nanocrystalline particle morphology with an average size of approximately 17 ± 0.5 nm. Figure 1(c)(d) presents the particle morphology of FeCoNiMoCe HEA/C from different angles, with the red region and its magnified image (Fig. 1(e)) labeled. The inset SAED pattern confirms the single crystallinity of the obtained FeCoNiMoCe HEA/C nanoparticles. The lattice spacing of 0.265 nm for the (111) planes is shown in the inset of Fig. 1(e). The Fast Fourier transform (FFT) patterns in Fig. 1(f) display distinct reflections of the HEA microcrystals on the (111) planes, consistent with the FFT patterns of pure crystals. Figure 1(g) reveals numerous dislocations and stacking faults. Additionally, the HAADF-STEM-EDS elemental mapping of the HEA in Fig. 1h and Fig. S7 shows a uniform distribution of Fe, Ni, Co, Mo, and Ce elements in the HEA nanostructure. The results demonstrate that high-entropy FeCoNiMoCe HEA/C nanoparticles were successfully prepared using a simple acid-catalyzed polymerization method. Additionally, we examined the detailed structures of FeCoNi/C and FeCoNiMo/C samples by TEM (Fig. S6(a)(b)).

Further X-ray photoelectron spectroscopy (XPS) analyses were conducted on FeCoNiMoCe HEA/C, FeCoNiMo/C, and FeCoNi/C to investigate their valence and surface chemistry. The XPS spectra confirmed the presence of Fe, Co, Ni, Mo, and Ce elements (Fig. 2a). These results are consistent with those obtained from energy-dispersive X-ray spectroscopy (EDS) and inductively coupled plasma (ICP) analysis. The high-resolution Fe 2p spectrum in Fig. 2b demonstrated a zero-valence state of Fe for FeCoNi/C (711.8 eV for Fe^0 $2p_{3/2}$ and 724.6 eV for Fe^0 $2p_{1/2}$). The Fe 2p spectrum of FeCoNiMo/C also displayed the existence of Fe^0 (711.2 eV for $2p_{3/2}$ and 724.4 eV for $2p_{1/2}$). The peaks at 708.4 and 722.2 eV for FeCoNiMoCe HEA/C belong to the metallic Fe^0 $2p_{3/2}$ and Fe^0 $2p_{1/2}$ peaks, respectively. [59]. The peaks at 781.1 and 796.8 eV for FeCoNi/C belong to the metallic Co^0 $2p_{3/2}$ and Co^0 $2p_{1/2}$ peaks, respectively. For FeCoNiMo/C, Co 2p spectrum (780.8 eV for Co^0 $2p_{3/2}$ and 796.6 eV for Co^0 $2p_{1/2}$). The Co 2p spectrum of FeCoNiMoCe HEA/C displayed the existence of Co^0 (779.9 eV for $2p_{3/2}$ and 795.1 eV for $2p_{1/2}$) (Fig. 2c) [60]. The Ni 2p spectrum in Fig. 2d displayed peaks at 855.5 eV for Ni^0 $2p_{3/2}$ and 873.3 eV for Ni^0 $2p_{1/2}$ (FeCoNi/C), the peaks at 855.3 eV for Ni^0 $2p_{3/2}$ and 872.1 eV for Ni^0 $2p_{1/2}$ (FeCoNiMo/C) and the peaks at 855.2 eV for Ni^0 $2p_{3/2}$ and 872.1 eV for Ni^0 $2p_{1/2}$ (FeCoNiMoCe HEA/C) [61]. In Fig. 2e, the presence of spin doublet peaks at 232.4 eV (Mo $3d_{5/2}$) and 235.3 eV (Mo $3d_{3/2}$) indicated the existence of metallic Mo in FeCoNiMo/C and FeCoNiMoCe HEA/C [62]. The high-resolution XPS spectrum of Ce 3d showed two peaks between 900–910 eV and 915–930 eV, which were identified as Ce $3d_{3/2}$, and a peak at 880–890 eV was assigned to Ce $3d_{5/2}$. These results indicated the coexistence of Ce^{3+} and Ce^{4+} in the FeCoNiMoCe HEA/C structure (as depicted in Fig. 4f) [63]. The binding energies of Fe^0, Co^0, Ni^0, and Mo^0 of FeCoNiMoCe HEA/C showed negative shifts compared with FeCoNiMo/C without Ce, indicating that the introduction of Ce in the FeCoNi/C alloy results in the movement of electrons on Fe, Co, Ni, and Mo surfaces. It is further evidence of a synergistic electronic

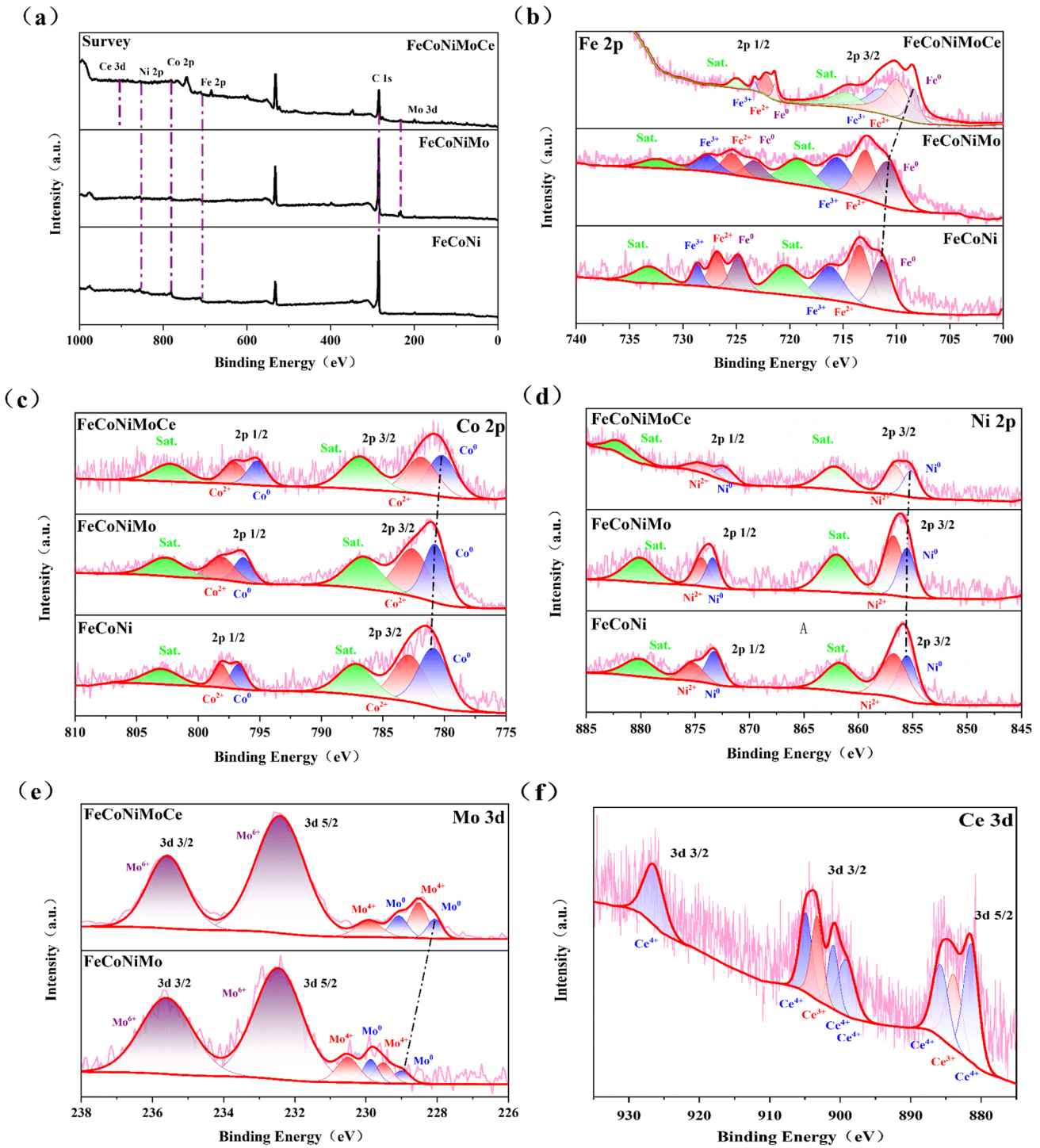

Fig. 2 High-resolution XPS spectra of FeCoNiMoCe HEA/C, FeCoNiMo/C and FeCoNi/C. **a** Survey XPS spectra of FeCoNiMoCe HEA/C, FeCoNiMo/C and FeCoNi/C; **b** Fe 2p of FeCoNiMoCe HEA/C, FeCoNiMo/C and FeCoNi/C; **c** Co 2p of FeCoNiMoCe HEA/C, FeCoNiMo/C and FeCoNi/C; **d** Ni 2p of FeCoNiMoCe HEA/C, FeCoNiMo/C and FeCoNi/C; **e** Mo 3d of FeCoNiMoCe HEA/C, FeCoNiMo/C; **f** Ce 3d of FeCoNiMoCe HEA/C

coupling effect among the Fe, Co, Ni, Mo, and Ce atoms, which may alter the adsorption of the HER and OER intermediates under the Co, Ni, Fe and Mo sites [64, 65].

An evaluation was conducted on the electrochemical performance of the prepared ternary FeCoNi/C, quaternary FeCoNiMo/C, and FeCoNiMoCe HEA/C in a 1.0 M KOH

three-electrode system, with commercial RuO2 used as a control for comparison. As shown in Fig. 3a, the ternary FeCoNi/C alloy exhibited an overpotential of 370 mV at a current density of 10 mA cm^{-2}, which was higher than that of commercial RuO_2 (300 mV). The overpotential of the quaternary FeCoNiMo/C alloy can be continuously reduced from 370 to 280 mV with the addition of Mo, which is 20 mV lower than that of commercial RuO_2. An excellent OER electrocatalyst is formed by adding the rare earth element Ce to form FeCoNiMoCe HEA/C, with an overpotential of only 260 mV, significantly lower than the commercial RuO_2 (300 mV). This improvement in catalytic activity may be attributed to the addition of an appropriate amount of Ce. Ce enhances the catalytic activity of the high entropy alloy by regulating the electronic structure of Fe, Co, Ni, and Mo, leading to changes in the lattice spacing of the alloy. As a result, the FeCoNiMoCe HEA/C exhibits moderate adsorption energy, achieving optimal performance [66]. The Tafel slope of FeCoNiMoCe HEA/C (63.4 mV dec^{-1}) is lower than that of FeCoNiMo/C (77.2 mV dec^{-1}), FeCoNi/C (110.5 mV dec^{-1}), and RuO_2 (101.6 mV dec-^{1}). Additionally, we compared the EIS of FeCoNi/C, FeCoNiMo/C, and FeCoNiMoCe HEA/C. As shown in Fig. 3c, FeCoNiMoCe HEA/C has the lowest charge transfer resistance, with R_{ct} and R_S values of 15 Ω and 1.25 Ω, respectively. In addition, we manually compensated the measured LSV curves using IR and compared the compensated and uncompensated FeCoNiMoCe HEA/C (Fig. S8a). We also compared the OER LSV curves and Tafel slopes of the compensated groups (Fig. S8b, c). The double-layer capacitance (C_{dl}) between the electrolyte and the electrocatalyst was calculated by cyclic voltammetry (Fig. S9), and the results are presented in Fig. 3d. The electrical double-layer capacitance (C_{dl}) of FeCoNiMoCe HEA/C is significantly higher (9.17 mF cm^{-2}) than that of FeCoNi/C (7.96 mF cm^{-2}) and FeCoNiMo/C (5.67 mF cm^{-2}), and slightly lower than that of RuO_2 (6.89 mF cm^{-2}).

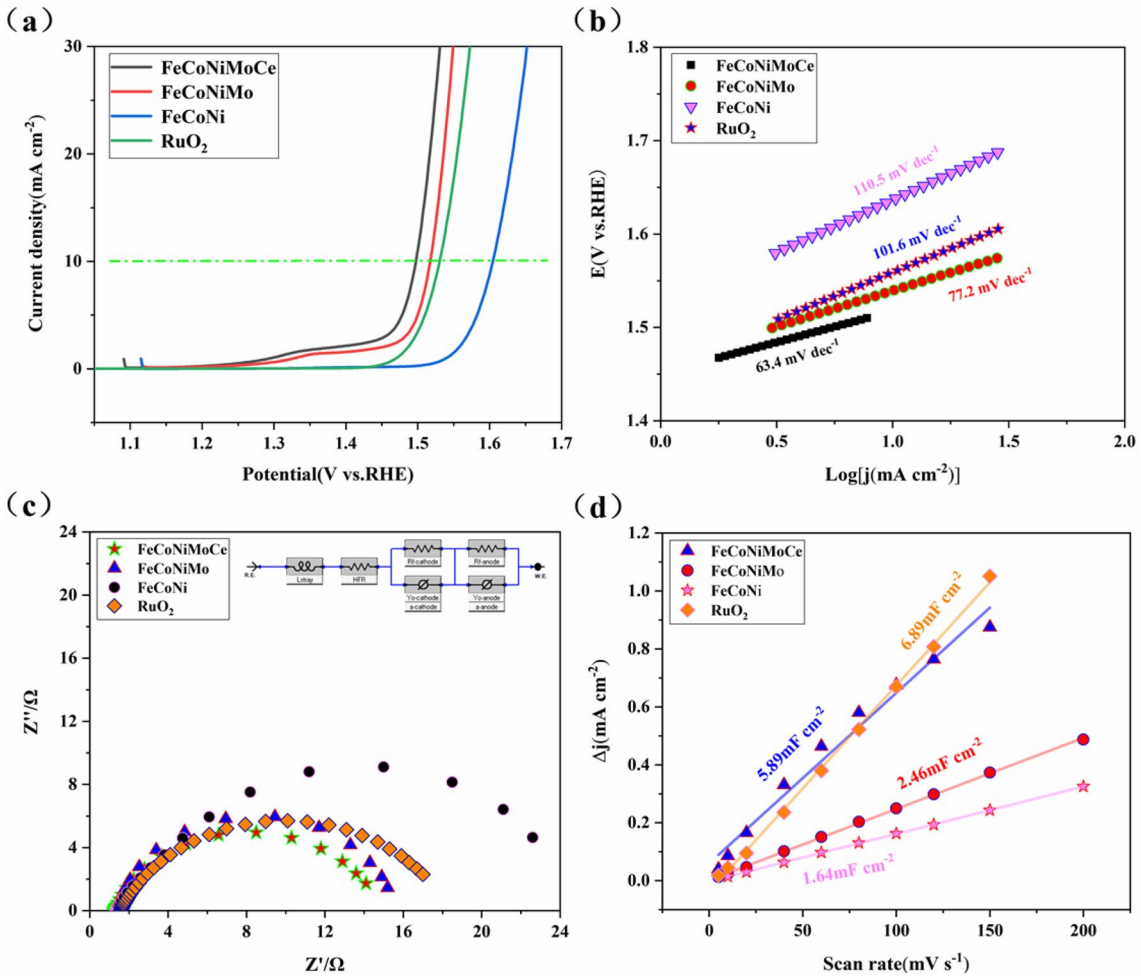

Fig. 3 **a** OER LSV curves of ternary FeCoNi/C, quaternary FeCoNiMo/C, quinary FeCoNiMoCe HEA/C, and the control RuO_2; **b** Tafel slopes of ternary FeCoNi/C, quaternary FeCoNiMo/C, quinary FeCoNiMoCe HEA/C, and the control RuO_2; **c** EIS measurements of ternary FeCoNi/C, quaternary FeCoNiMo/C, quinary FeCoNiMoCe HEA/C, and the control RuO_2; **d** C_{dl} values obtained by fitting the CV curves of ternary FeCoNi/C, quaternary FeCoNiMo/C, quinary FeCoNiMoCe HEA/C, and the control RuO_2

As shown in Fig. 4a, with the increase of metal elements, the ECSA also significantly expands. The ECSA of FeCoNiMoCe HEA/C (229.3 cm^2 mg^{-1}) is approximately 1.61 times larger than that of FeCoNi/C (141.8 cm^2 mg^{-1}) and 1.2 times larger than that of FeCoNiMo/C (119.0 cm^2 mg^{-1}). Furthermore, the current density of ECSA is normalized to reveal the intrinsic surface area catalytic activity of these catalysts. FeCoNiMoCe HEA/C still exhibits the highest OER catalytic activity (Fig. 4b). It can also be seen from Fig. S8d that under the same conditions, FeCoNiMoCe HEA/C outperforms many previously reported non-precious metal OER high-entropy electrocatalysts.

We also evaluated the HER activity of ternary FeCoNi/C, quaternary FeCoNiMo/C, and FeCoNiMoCe HEA/C in 1.0 M KOH. Similar to the OER performance, the HER activity improved with an increase in the number of metal species. Specifically, the overpotential at 10 mA cm^{-2} decreased from 440 mV for FeCoNi/C to 250 mV for quaternary FeCoNiMo/C and 130 mV for FeCoNiMoCe HEA/C (Fig. 5a). Additionally, as a commercial electrocatalyst, the overpotential of Pt/C at 10 mA cm^{-2} was only 60 mV lower than that of FeCoNiMoCe HEA/C, indicating the promising potential for large-scale use of FeCoNiMoCe HEA/C. The Tafel slope of FeCoNiMoCe HEA/C was 94.4 mV dec^{-1} (Fig. 5b), significantly lower than that of ternary FeCoNi/C (187.9 mV dec-1) and quaternary FeCoNiMo/C (161.3 mV dec^{-1}). As a commercial catalyst, we separately tested the EIS and CV of Pt/C and calculated its C_{dl} based on the CV (Fig. S10). The HER LSV curves of FeCoNi/C, FeCoNiMo/C, and FeCoNiMoCe HEA/C after IR compensation, as well as the Tafel slope, are shown in Fig. S11. Figure 5c presents the HER ECSA normalized curves of ternary FeCoNi/C, quaternary FeCoNiMo/C, and FeCoNiMoCe HEA/C, comparing the overpotential at 10 mA cm^{-2} with various reported non-precious metal materials. It is found that FeCoNiMoCe HEA/C is comparable to some excellent candidate materials.

The turnover frequency (TOF) values were also employed to evaluate the catalytic activities of all samples toward the HER and the OER [67]. As presented in Fig. 6, the TOF value of FeCoNiMoCe HEA/C catalyst towards OER is calculated to be 0.158 s^{-1} at an overpotential of 1.55 V, which is much larger than that of RuO_2 (0.117 s^{-1}), FeCoNiMo/C (0.07 s^{-1}), and FeCoNi/C (0.006 s^{-1}) catalysts. As for the HER, the FeCoNiMoCe HEA/C catalyst presents a TOF value of 0.522 s^{-1} at an overpotential of 0.3 V, which is also significantly superior to Pt/C (0.401 s^{-1}), FeCoNiMo/C (0.184 s^{-1}), and FeCoNi/C (0.025 s^{-1}) catalysts.

The FeCoNiMoCe HEA/C catalyst demonstrates excellent stability for 12 h at a voltage of 1.55 V, as shown in Fig. 7a. Additionally, during the 12-h measurement at a current density of 20 mA cm^{-2}, the fluctuation is only about 1 mA, as seen in Fig. 7b. These results suggest that the FeCoNiMoCe HEA/C catalyst is highly stable.

The stability of electrocatalysts over time depends on the structure of the active material and surface reconstruction after prolonged use. To investigate the morphological and surface chemical changes of the FeCoNiMoCe HEA/C catalyst after stability testing, various characterization techniques including FESEM and TEM were employed. The nanoparticle morphology of the FeCoNiMoCe HEA/C catalyst was found to be maintained after stability testing, as shown in Fig. 8a. Figure 8b shows the high-entropy alloy (HEA) of the FeCoNiMoCe HEA/C (HEA) sample after 12 h of stability testing, along with the newly formed high-entropy oxide (HEO). HRTEM images in Fig. 8c–d reveal the interplanar spacing of HEO and the presence of numerous dislocations and stacking faults, indicating that the

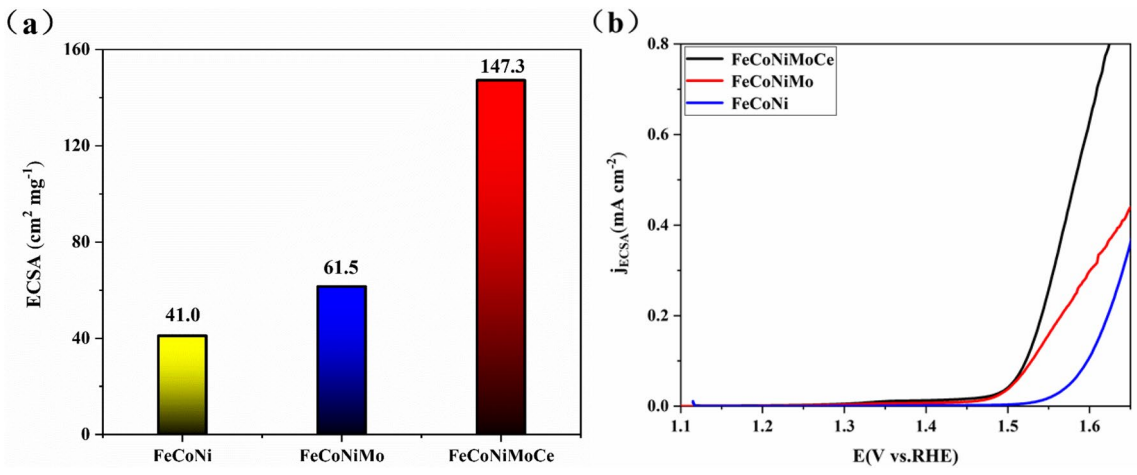

Fig. 4 **a** ECSA (Electrochemically Active Surface Area) of ternary FeCoNi/C, quaternary FeCoNiMo/C, quinary FeCoNiMoCe HEA/C and RuO_2; **b** ECSA-normalized OER LSV curves of nary FeCoNi/C, quaternary FeCoNiMo/C, quinary FeCoNiMoCe HEA/C and RuO_2

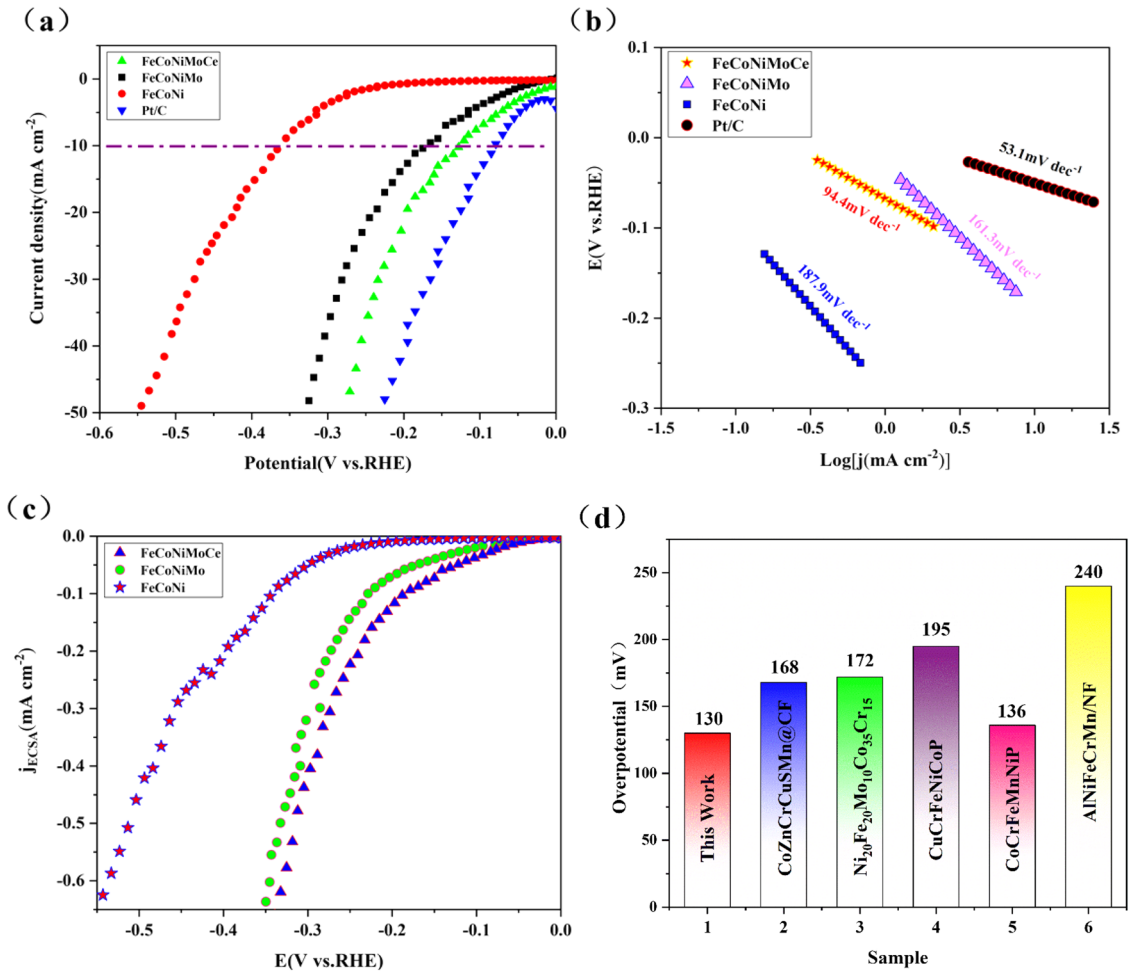

Fig. 5 **a** HER LSV curves of ternary FeCoNi/C, quaternary FeCoNiMo/C, quinary FeCoNiMoCe HEA/C, and the control RuO_2; **b** Tafel slopes of ternary FeCoNi/C, quaternary FeCoNiMo/C, quinary FeCoNiMoCe HEA/C, and the control Pt/C; **c** ECSA-normalized HER LSV curves of nary FeCoNi/C, quaternary FeCoNiMo/C, and quinary FeCoNiMoCe HEA/C; **d** Comparison of the overpotentials of HER performance to drive a current density of 10 mA cm^{-2} for the FeCoNiMoCe HEA/C with recently reported electrocatalysts

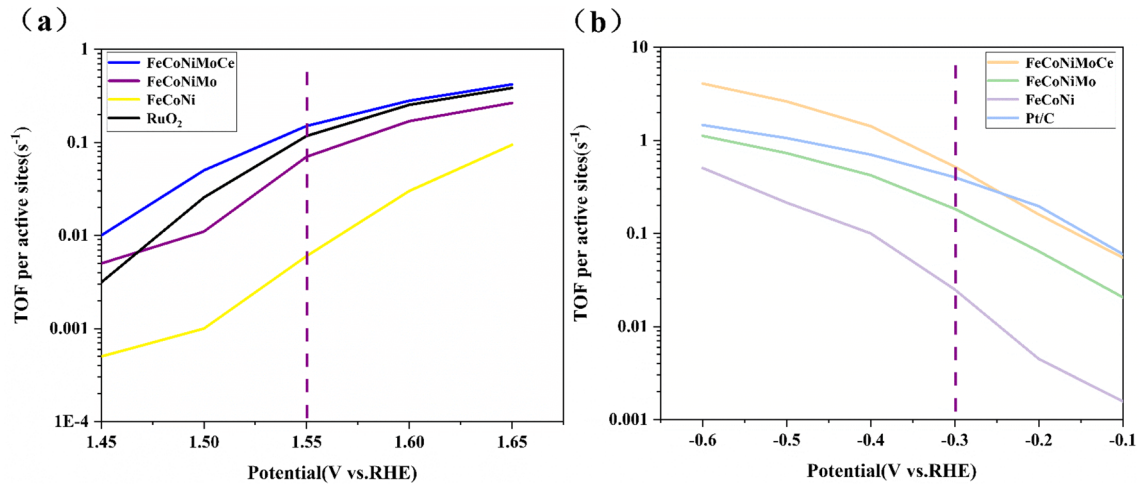

Fig. 6 TOF curves of different samples for (**a**) HER and (**b**) OER

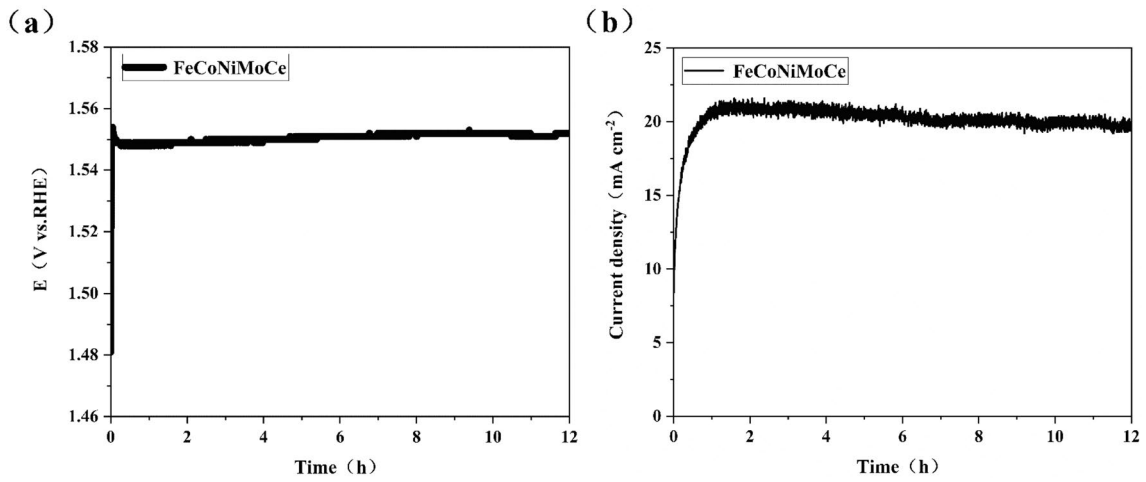

Fig. 7 **a** Chronopotentiometry responses (E–t) of FeCoNiMoCe HEA/C; **b** Chronoamperometric responses (I–t) of FeCoNiMoCe HEA/C

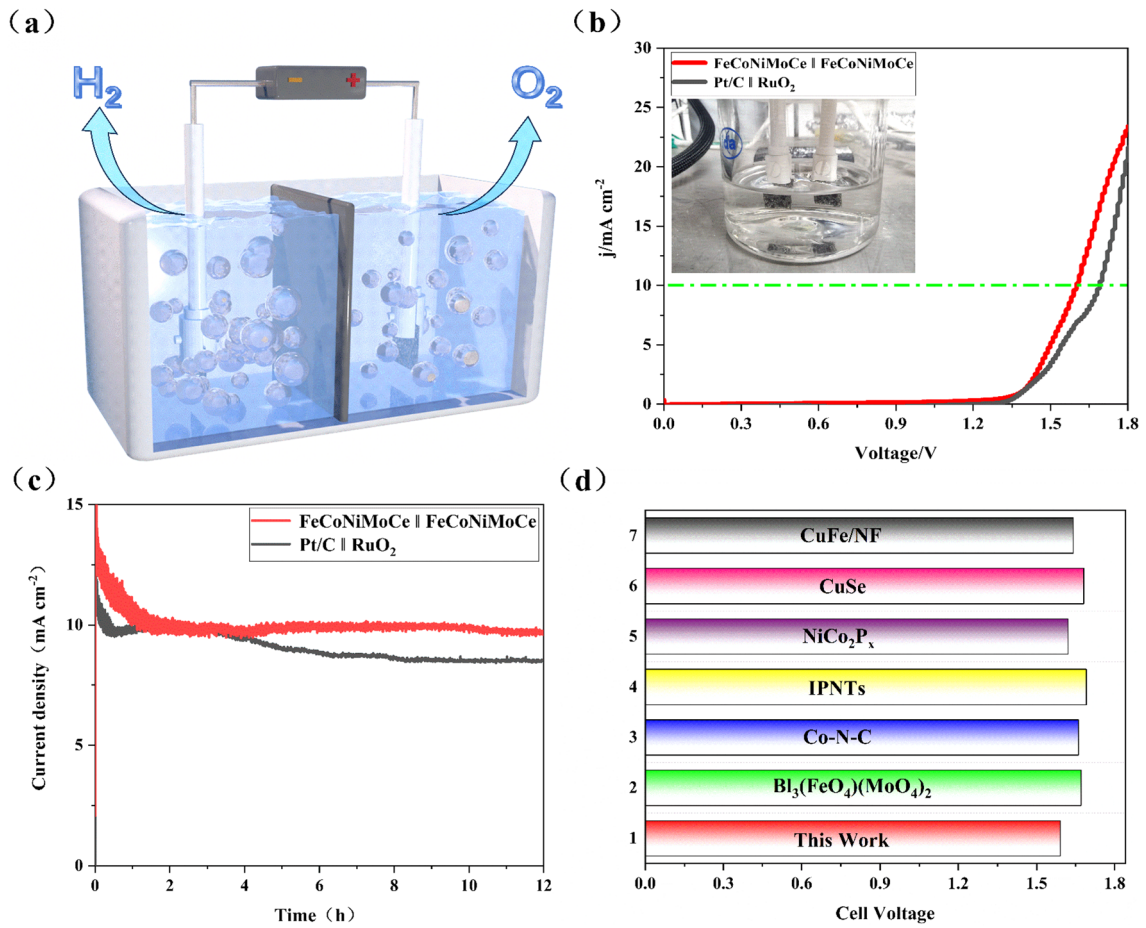

Fig. 8 **a** Schematic diagram of the overall water splitting device; **b** overall water splitting performance of FeCoNiMoCe‖FeCoNiMoCe and Pt/C‖RuO_2 electrode pairs. Insets: Schematic diagram of complete water splitting using FeCoNiMoCe HEA/C catalyst as both electrodes; **c** chronoamperometric responses (I–t) of FeCoNiMoCe HEA/C and (Pt/C‖RuO_2); **d** performance of FeCoNiMoCe HEA/C electrolyzer compared with reported water splitting catalysts

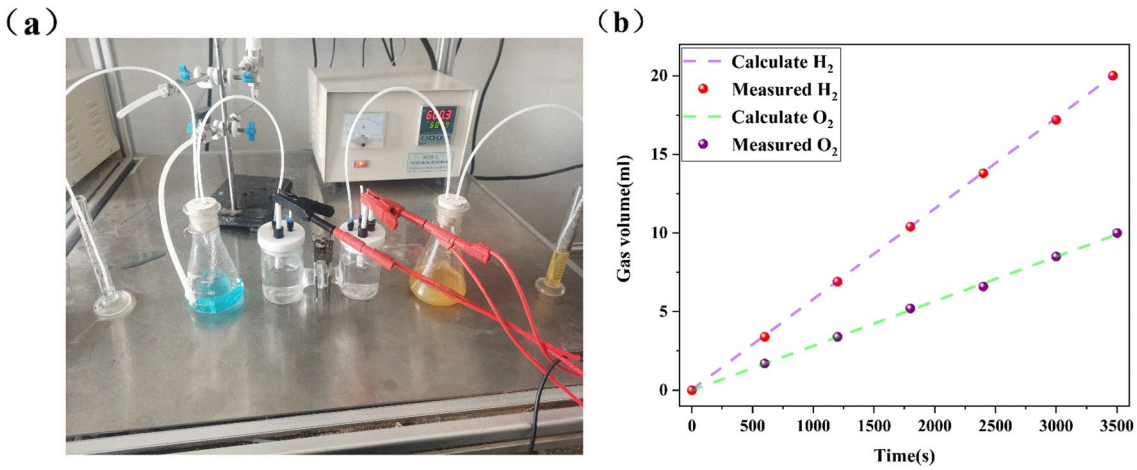

Fig. 9 **a** H_2 and O_2 gas collection device; **b** amount of H_2 and O_2 between experimental and the theoretical

structure of the HEA has been partially preserved while new oxides have formed after prolonged stability testing. Based on the HAADF-STEM-EDS analysis presented in Fig. 8e, the Fe, Co, Ni, Mo, Ce, and O elements of the FeCoNiMoCe HEA/C catalyst are evenly dispersed throughout the entire region following stability testing.

After demonstrating that the FeCoNiMoCe HEA/C catalyst has good OER and HER activity and stability, a two-electrode electrolysis cell was assembled to verify the performance of FeCoNiMoCe HEA/C for the total hydrolysis of water, which is shown schematically in Fig. 8a. We also used Pt/C||RuO_2 as a commercial reference, and the results are shown in Fig. 8b. For the FeCoNiMoCe||FeCoNiMoCe catalyst, a current density of 10 mA cm^{-2} was achieved at only 1.59 V, which was about 100 mV lower than Pt/C||RuO_2 (1.69 V). Stability testing was conducted at 1.7 V for both FeCoNiMoCe||FeCoNiMoCe and Pt/C||RuO_2 (Fig. 8c), and it can be observed that FeCoNiMoCe||FeCoNiMoCe maintained good stability, surpassing Pt/C||RuO_2. Interestingly, the FeCoNiMoCe HEA/C dual-electrode electrolyzer also outperformed many previously reported advanced catalysts (Fig. 8d). Additionally, we compared the OER, HER, and overall water splitting performance of the FeCoNi/C, FeCoNiMo/C, and FeCoNiMoCe HEA/C catalysts we prepared under conditions of 10 mA cm^{-2} with the latest literature-reported excellent catalysts. Our findings indicate that the FeCoNiMoCe HEA/C catalyst also outperforms many recently reported non-precious metal high-entropy material electrocatalysts (Table S2) [33, 68–72].

In order to investigate the Faraday efficiency of the FeCoNiMoCe HEA/C, a drainage system presented in Fig. 9 a was adopted to collect the gases and evaluate the overall water splitting behavior in a more practical application. As shown, the collected amount of H_2 and O_2 constantly evolves in a stoichiometric proportion of 2:1 (Fig. 7 b). Acquisition of 20 mL H_2 is realized within approximately 3468 s, with a Faradaic efficiency (FE) of almost 99.58%. Whereas the harvest of 10 mL O_2 is realized within approximately 3502 s, with a Faradaic efficiency (FE) of almost 98.4% [73].

Finally, a brief analysis of the active sites of FeCoNiMoCe HEA/C was conducted based on the results of the literature testing. Compared to doping transition metals, introducing rare earth element cerium (Ce) with unique 4f orbitals as an external atom into the valence orbitals between Fe, Co, Ni, and Mo, combined with surface decoration to expose more active sites and high-entropy coordination to enhance intrinsic activity and structural stability, improves the activity and durability of the catalyst. This provides a novel design for HEA catalysts [74]. According to the consulted literature, FeCoNiCuCe high-entropy alloy nanoparticles (NPs) can effectively drive non-active Ce to electron-enriched active sites through strong local electronic interactions caused by electronegativity differences between low electronegativity Ce and high electronegativity Mo with Fe, Co, and Ni metals. This reduces the adsorption energy of reactants, intermediates, and products, enhancing the activities of the hydrogen evolution reaction (HER) and oxygen evolution reaction (OER) of the HEA [75–78].

Conclusions

In summary, we synthesized a high-entropy alloy using the critical acid polymerization method and calcination-reduction method. By incorporating unique rare earth elements (Ce) into the FeCoNiMo/C, the catalytic performance of the water electrolysis catalyst was significantly enhanced. The

FeCoNiMoCe HEA/C nanoparticles can be used as dual-function catalysts, thanks to the high-entropy materials and rare earth elements. The catalyst's excellent catalytic activity is a result of the mixing of different atoms and the diversity of components, which induce synergistic effects. It exhibits outstanding electrocatalytic performance in both the oxygen evolution reaction (OER) and hydrogen evolution reaction (HER), surpassing most recently reported multifunctional electrocatalysts. This research expands the synthetic strategies for high-entropy compounds and provides a method for the rational design and manufacture of high-entropy electrocatalysts in the energy and catalysis fields.

Supplementary Information The online version contains supplementary material available at https://doi.org/10.1007/s11581-024-05532-2.

Acknowledgements This work was supported by the National Natural Science Foundation of China (51864040, 51962028, 52162010); Inner Mongolia Autonomous Region Science and Technology Program (2021GG0042); Inner Mongolia Autonomous Region Youth Science and Technology Excellence in Higher Education (NJYT22064); Inner Mongolia Autonomous Region Natural Science Foundation Program (2022MS05018, 2022LHMS05021)).

Author contribution ZWY made substantial contributions to the conception and design of the work the acquisition; GRH drafted the work and revised it critically for important intellectual content; YQX analyses and interpretation of data; HYR agree to be accountable for all aspects of the work in ensuring that questions related to the accuracy and integrity of any part of the work are appropriately investigated and resolved; Z.GF and GLL create of new software used in the work. All authors reviewed the manuscript.

Data availability No datasets were generated or analyzed during the current study.

Declarations

Competing interests The authors declare no competing interests.

References

1. Tong Y, Feng D, Chen P (2021) Dual modification strategy of nickel sulfide as ph-universal catalysts for hydrogen production at large current density[J]. ACS Sustain Chem Eng 9(31):10601–10610. https://doi.org/10.1021/acssuschemeng.1c02807
2. Feng D, Ye R, Tong Y et al (2023) Engineering cobalt molybdate nanosheet arrays with phosphorus-modified nickel as heterogeneous electrodes for highly-active energy-saving water splitting[J]. J Colloid Interface Sci 636:425–434. https://doi.org/10.1016/j.jcis.2023.01.045
3. Li K, Tong Y, He J et al (2023) Anion-modulated CoP electrode as bifunctional electrocatalyst for anion-exchange membrane hydrazine-assisted water electrolyser[J]. Mater Horiz 10(11):5277–5287. https://doi.org/10.1039/D3MH00872J
4. Ren X, Tong Y (2024) The self-reconstruction of Co-modified bimetallic hydroxysulfide nanosheet arrays for efficient hydrazine assisted water splitting[J]. Int J Hydrog Energy 49:489–497. https://doi.org/10.1016/j.ijhydene.2023.08.109
5. Yan H, Xie Y, Wu A et al (2019) Anion-modulated HER and OER activities of 3D Ni–V-based interstitial compound heterojunctions for high-efficiency and stable overall water splitting[J]. Adv Mater 31(23):1901174. https://doi.org/10.1002/adma.201901174
6. Zheng Z, Yu L, Gao M et al (2020) Boosting hydrogen evolution on MoS2 via co-confining selenium in surface and cobalt in inner layer[J]. Nat Commun 11(1):3315. https://doi.org/10.1038/s41467-020-17199-0
7. Li Z, Liu D, Lu X et al (2022) Boosting oxygen evolution of layered double hydroxide through electronic coupling with ultralow noble metal doping[J]. Dalton Trans 51(4):1527–1532. https://doi.org/10.1039/D1DT03906G
8. Tian L, Li Z, Xu X et al (2021) Advances in noble metal (Ru, Rh, and Ir) doping for boosting water splitting electrocatalysis[J]. J Mater Chem A 9(23):13459–13470. https://doi.org/10.1039/D1TA01108A
9. Xu H, Shang H, Liu Q et al (2021) Dual mode electrochemical-photoelectrochemical sensing platform for hydrogen sulfide detection based on the inhibition effect of titanium dioxide/bismuth tungstate/silver heterojunction[J]. J Colloid Interface Sci 581:323–333. https://doi.org/10.1016/j.jcis.2020.07.120
10. Xu H, Shang H, Wang C et al (2020) Surface and interface engineering of noble-metal-free electrocatalysts for efficient overall water splitting[J]. Coord Chem Rev 418:213374. https://doi.org/10.1016/j.ccr.2020.213374
11. Bao J, Zhang X, Fan B et al (2015) Ultrathin spinel-structured nanosheets rich in oxygen deficiencies for enhanced electrocatalytic water oxidation[J]. Angew Chem Int Ed 54(25):7399–7404. https://doi.org/10.1002/anie.201502226
12. Tan Y, Wang H, Liu P et al (2016) Versatile nanoporous bimetallic phosphides towards electrochemical water splitting[J]. Energy Environ Sci 9(7):2257–2261. https://doi.org/10.1039/C6EE01109H
13. Tang T, Jiang W-J, Niu S et al (2017) Electronic and morphological dual modulation of cobalt carbonate hydroxides by mn doping toward highly efficient and stable bifunctional electrocatalysts for overall water splitting[J]. J Am Chem Soc 139(24):8320–8328. https://doi.org/10.1021/jacs.7b03507
14. Tian L, Zhai X, Wang X et al (2020) Advances in manganese-based oxides for oxygen evolution reaction[J]. J Mater Chem A 8(29):14400–14414. https://doi.org/10.1039/D0TA05116K
15. Wang C, Jin L, Shang H et al (2021) Advances in engineering RuO2 electrocatalysts towards oxygen evolution reaction[J]. Chin Chem Lett 32(7):2108–2116. https://doi.org/10.1016/j.cclet.2020.11.051
16. Xiong B, Chen L, Shi J (2018) Anion-containing noble-metal-free bifunctional electrocatalysts for overall water splitting[J]. ACS Catal 8(4):3688–3707. https://doi.org/10.1021/acscatal.7b04286
17. Zhang Y, Ouyang B, Xu J et al (2016) Rapid synthesis of cobalt nitride nanowires: highly efficient and low-cost catalysts for oxygen evolution[J]. Angew Chem Int Ed 55(30):8670–8674. https://doi.org/10.1002/anie.201604372
18. Zhu C, Shi Q, Feng S et al (2018) Single-atom catalysts for electrochemical water splitting[J]. ACS Energy Lett 3(7):1713–1721. https://doi.org/10.1021/acsenergylett.8b00640
19. Zhu YP, Ma TY, Jaroniec M et al (2017) Self-templating synthesis of hollow Co3O4 microtube arrays for highly efficient water electrolysis[J]. Angew Chem Int Ed 56(5):1324–1328. https://doi.org/10.1002/anie.201610413
20. Udayakumar A, Dhandapani P, Ramasamy S et al (2024) Recent developments in noble metal–based hybrid electrocatalysts for overall water splitting[J]. Ionics 30(1):61–84. https://doi.org/10.1007/s11581-023-05269-4
21. Tong Y, Mao H, Xu Y et al (2019) Oxygen vacancies confined in Co3O4 quantum dots for promoting oxygen evolution

electrocatalysis[J]. Inorg Chem Front 6(8):2055–2060. https://doi.org/10.1039/C9QI00325H
22. Cheng X, Tong Y (2023) Hierarchical cobalt–nickel phosphide/molybdenum disulfide hybrid electrocatalyst triggering efficient hydrogen generation in a wider pH range[J]. ACS Appl Energy Mater 6(18):9577–9584. https://doi.org/10.1021/acsaem.3c01599
23. Cheng X, Tong Y (2023) Interface coupling of cobalt hydroxide/molybdenum disulfide heterostructured nanosheet arrays for highly efficient hydrazine-assisted hydrogen generation[J]. ACS Sustain Chem Eng 11(8):3219–3227. https://doi.org/10.1021/acssuschemeng.2c05636
24. Vasileff A, Xu C, Jiao Y et al (2018) Surface and interface engineering in copper-based bimetallic materials for selective CO2 electroreduction[J]. Chem 4(8):1809–1831. https://doi.org/10.1016/j.chempr.2018.05.001
25. Wang Z, Shen S, Lin Z et al (2022) Regulating the local spin state and band structure in Ni3S2 nanosheet for improved oxygen evolution activity[J]. Adv Funct Mater 32(18):2112832. https://doi.org/10.1002/adfm.202112832
26. Lin Z, Wang Z, Gong J et al (2023) Reversed spillover effect activated by Pt atom dimers boosts alkaline hydrogen evolution reaction[J]. Adv Funct Mater 33(45):2307510. https://doi.org/10.1002/adfm.202307510
27. Li Y, Sun Q (2016) Recent advances in breaking scaling relations for effective electrochemical conversion of CO2[J]. Adv Energy Mater 6(17):1600463. https://doi.org/10.1002/aenm.201600463
28. Wen L, Zhang X, Liu J et al (2019) Cr-dopant induced breaking of scaling relations in CoFe layered double hydroxides for improvement of oxygen evolution reaction[J]. Small 15(35):1902373. https://doi.org/10.1002/smll.201902373
29. Tomboc GM, Kwon T, Joo J et al (2020) High entropy alloy electrocatalysts: a critical assessment of fabrication and performance[J]. J Mater Chem A 8(30):14844–14862. https://doi.org/10.1039/D0TA05176D
30. Ye YF, Wang Q, Lu J et al (2016) High-entropy alloy: challenges and prospects[J]. Mater Today 19(6):349–362. https://doi.org/10.1016/j.mattod.2015.11.026
31. Zhang G, Ming K, Kang J et al (2018) High entropy alloy as a highly active and stable electrocatalyst for hydrogen evolution reaction[J]. Electrochim Acta 279:19–23. https://doi.org/10.1016/j.electacta.2018.05.035
32. Lin Z, Xiao B, Huang M et al (2022) Realizing negatively charged metal atoms through controllable d-electron transfer in ternary Ir1−xRhxSb intermetallic alloy for hydrogen evolution reaction[J]. Adv Energy Mater 12(25):2200855. https://doi.org/10.1002/aenm.202200855
33. Lai D, Kang Q, Gao F et al (2021) High-entropy effect of a metal phosphide on enhanced overall water splitting performance[J]. J Mater Chem A 9(33):17913–17922. https://doi.org/10.1039/D1TA04755H
34. Liu H, Syama L, Zhang L et al (2021) High-entropy alloys and compounds for electrocatalytic energy conversion applications[J]. SusMat 1(4):482–505. https://doi.org/10.1002/sus2.32
35. Zhang Y, Wang D, Wang S (2022) High-entropy alloys for electrocatalysis: design, characterization, and applications[J]. Small 18(7):2104339. https://doi.org/10.1002/smll.202104339
36. Du H, Kong R-M, Guo X et al (2018) Recent progress in transition metal phosphides with enhanced electrocatalysis for hydrogen evolution[J]. Nanoscale 10(46):21617–21624. https://doi.org/10.1039/C8NR07891B
37. Chen S, Huang H, Jiang P et al (2020) Mn-doped RuO2 nanocrystals as highly active electrocatalysts for enhanced oxygen evolution in acidic media[J]. ACS Catal 10(2):1152–1160. https://doi.org/10.1021/acscatal.9b04922
38. Zagalskaya A, Alexandrov V (2020) Role of defects in the interplay between adsorbate evolving and lattice oxygen mechanisms of the oxygen evolution reaction in RuO2 and IrO2[J]. ACS Catal 10(6):3650–3657. https://doi.org/10.1021/acscatal.9b05544
39. Fang M, Gao W, Dong G et al (2016) Hierarchical NiMo-based 3D electrocatalysts for highly-efficient hydrogen evolution in alkaline conditions[J]. Nano Energy 27:247–254. https://doi.org/10.1016/j.nanoen.2016.07.005
40. Jaksic MM (2001) Hypo–hyper-d-electronic interactive nature of interionic synergism in catalysis and electrocatalysis for hydrogen reactions[J]. Int J Hydrog Energy 26(6):559–578. https://doi.org/10.1016/S0360-3199(00)00120-8
41. Hasija V, Raizada P, Sudhaik A et al (2019) Recent advances in noble metal free doped graphitic carbon nitride based nanohybrids for photocatalysis of organic contaminants in water: a review[J]. Appl Mater Today 15:494–524. https://doi.org/10.1016/j.apmt.2019.04.003
42. Liu X, Yan C-H, Capobianco JA (2015) Photon upconversion nanomaterials[J]. Chem Soc Rev 44(6):1299–1301. https://doi.org/10.1039/C5CS90009C
43. Li J, Zhu Y, Chen W et al (2019) Breathing-mimicking electrocatalysis for oxygen evolution and reduction[J]. Joule 3(2):557–569. https://doi.org/10.1016/j.joule.2018.11.015
44. Rosalbino F, Macciò D, Angelini E et al (2005) Electrocatalytic properties of Fe–R (R=rare earth metal) crystalline alloys as hydrogen electrodes in alkaline water electrolysis[J]. J Alloys Compd 403(1):275–282. https://doi.org/10.1016/j.jallcom.2005.03.075
45. Li K, He J, Guan X et al (2023) Phosphorus-modified amorphous high-entropy CoFeNiCrMn compound as high-performance electrocatalyst for hydrazine-assisted water electrolysis[J]. Small 19(42):2302130. https://doi.org/10.1002/smll.202302130
46. Li K, Zhou G, Tong Y et al (2023) Interface engineering of a hierarchical P-modified Co/Ni3P heterostructure for highly efficient water electrolysis coupled with hydrazine degradation[J]. ACS Sustain Chem Eng 11(38):14186–14196. https://doi.org/10.1021/acssuschemeng.3c03909
47. He QF, Wang JG, Chen HA et al (2022) A highly distorted ultraelastic chemically complex Elinvar alloy[J]. Nature 602(7896):251–257. https://doi.org/10.1038/s41586-021-04309-1
48. Li H, Zhu H, Shen Q et al (2021) A novel synergistic confinement strategy for controlled synthesis of high-entropy alloy electrocatalysts[J]. Chem Commun 57(21):2637–2640. https://doi.org/10.1039/D0CC07345H
49. Sivanantham A, Lee H, Hwang SW et al (2021) Preparation, electrical and electrochemical characterizations of CuCoNiFeMn high-entropy-alloy for overall water splitting at neutral-pH[J]. J Mater Chem A 9(31):16841–16851. https://doi.org/10.1039/D1TA02621F
50. Ma Y, Ma Y, Wang Q et al (2021) High-entropy energy materials: challenges and new opportunities[J]. Energy Environ Sci 14(5):2883–2905. https://doi.org/10.1039/D1EE00505G
51. Yao Y, Huang Z, Xie P et al (2018) Carbothermal shock synthesis of high-entropy-alloy nanoparticles[J]. Science 359(6383):1489–1494. https://doi.org/10.1126/science.aan5412
52. Bondesgaard M, Broge NLN, Mamakhel A et al (2019) General solvothermal synthesis method for complete solubility range bimetallic and high-entropy alloy nanocatalysts[J]. Adv Funct Mater 29(50):1905933. https://doi.org/10.1002/adfm.201905933
53. Niu B, Zhang F, Ping H et al (2017) Sol-gel autocombustion synthesis of nanocrystalline high-entropy alloys[J]. Sci Rep 7(1):3421. https://doi.org/10.1038/s41598-017-03644-6
54. Gao S, Hao S, Huang Z et al (2020) Synthesis of high-entropy alloy nanoparticles on supports by the fast moving bed pyrolysis[J]. Nat Commun 11(1):2016. https://doi.org/10.1038/s41467-020-15934-1
55. Wu D, Kusada K, Yamamoto T et al (2020) Platinum-group-metal high-entropy-alloy nanoparticles[J]. J Am Chem Soc 142(32):13833–13838. https://doi.org/10.1021/jacs.0c04807

56. Wu K, Wang X-Y, Guo L-L et al (2020) Facile synthesis of Au embedded CuOx-CeO2 core/shell nanospheres as highly reactive and sinter-resistant catalysts for catalytic hydrogenation of p-nitrophenol[J]. Nano Res 13(8):2044–2055. https://doi.org/10.1007/s12274-020-2806-9
57. Phienluphon R, Ai P, Gao X et al (2016) Direct fabrication of catalytically active FexC sites by sol–gel autocombustion for preparing Fischer-Tropsch synthesis catalysts without reduction[J]. Catal Sci Technol 6(20):7597–7603. https://doi.org/10.1039/C6CY01383J
58. Zhao X, Xue Z, Chen W et al (2020) Eutectic synthesis of high-entropy metal phosphides for electrocatalytic water splitting[J]. ChemSusChem 13(8):2038–2042. https://doi.org/10.1002/cssc.202000173
59. Romero J, Varela M, Assebban M et al (2020) Insights into the formation of metal carbon nanocomposites for energy storage using hybrid NiFe layered double hydroxides as precursors[J]. Chem Sci 11(29):7626–7633. https://doi.org/10.1039/D0SC00697A
60. Song H, Wu M, Tang Z et al (2021) Single atom ruthenium-doped CoP/CDs nanosheets via splicing of carbon-dots for robust hydrogen production[J]. Angew Chem Int Ed 60(13):7234–7244. https://doi.org/10.1002/anie.202017102
61. Wang Y, Tao S, Lin H et al (2021) Atomically targeting NiFe LDH to create multivacancies for OER catalysis with a small organic anchor[J]. Nano Energy 81:105606. https://doi.org/10.1016/j.nanoen.2020.105606
62. Luo M, Zhao Z, Zhang Y et al (2019) PdMo bimetallene for oxygen reduction catalysis[J]. Nature 574(7776):81–85. https://doi.org/10.1038/s41586-019-1603-7
63. Xu H, Wang B, Shan C et al (2018) Ce-doped NiFe-layered double hydroxide ultrathin nanosheets/nanocarbon hierarchical nanocomposite as an efficient oxygen evolution catalyst[J]. ACS Appl Mater Interfaces 10(7):6336–6345. https://doi.org/10.1021/acsami.7b17939
64. Tao HB, Xu Y, Huang X et al (2019) A general method to probe oxygen evolution intermediates at operating conditions[J]. Joule 3(6):1498–1509. https://doi.org/10.1016/j.joule.2019.03.012
65. Zhang Y, Zhu X, Zhang G et al (2021) Rational catalyst design for oxygen evolution under acidic conditions: strategies toward enhanced electrocatalytic performance[J]. J Mater Chem A 9(10):5890–5914. https://doi.org/10.1039/D0TA11982B
66. Chen S, Wang Y, Wang Z et al (2023) Advances in nonprecious metal catalysts for efficient water oxidation in alkaline media[J]. Ionics 29(1):9–32. https://doi.org/10.1007/s11581-022-04774-2
67. Zeng L, Sun K, Wang X et al (2018) Three-dimensional-networked Ni2P/Ni3S2 heteronanoflake arrays for highly enhanced electrochemical overall-water-splitting activity[J]. Nano Energy 51:26–36. https://doi.org/10.1016/j.nanoen.2018.06.048
68. Zhang Q, Lian K, Liu Q et al (2023) High entropy alloy nanoparticles as efficient catalysts for alkaline overall seawater splitting and Zn-air batteries[J]. J Colloid Interface Sci 646:844–854. https://doi.org/10.1016/j.jcis.2023.05.074
69. Huo X, Zuo X, Wang X et al (2023) High entropy alloy CoCrFeNiMo reinforced electrocatalytic performance for high-efficient electrocatalytic water splitting[J]. Chem Asian J 18(15):e202300456. https://doi.org/10.1002/asia.202300456
70. Lei Y, Zhang L, Xu W et al (2022) Carbon-supported high-entropy Co-Zn-Cd-Cu-Mn sulfide nanoarrays promise high-performance overall water splitting[J]. Nano Res 15(7):6054–6061. https://doi.org/10.1007/s12274-022-4304-8
71. Wang Z, Han S, Zhang Y et al (2024) Decorated NiFeOOH on high entropy perovskite oxide by interface engineering for efficient oxygen evolution and overall water splitting[J]. Fuel 357:129946. https://doi.org/10.1016/j.fuel.2023.129946
72. Wang S, Huo W, Fang F et al (2022) High entropy alloy/C nanoparticles derived from polymetallic MOF as promising electrocatalysts for alkaline oxygen evolution reaction[J]. Chem Eng J 429:132410. https://doi.org/10.1016/j.cej.2021.132410
73. Wang L, Xue X, Luan Q et al (2023) Interface engineering of Mo-doped Ni9S8/Ni3S2 multiphase heterostructure nanoflowers by one step synthesis for efficient overall water splitting[J]. J Colloid Interface Sci 634:563–574. https://doi.org/10.1016/j.jcis.2022.12.064
74. Zeng K, Zhang J, Gao W et al (2022) Surface-decorated high-entropy alloy catalysts with significantly boosted activity and stability[J]. Adv Funct Mater 32(33):2204643. https://doi.org/10.1002/adfm.202204643
75. Zhu H, Sun S, Hao J et al (2023) A high-entropy atomic environment converts inactive to active sites for electrocatalysis[J]. Energy Environ Sci 16(2):619–628. https://doi.org/10.1039/D2EE03185J
76. Feng G, Pan Y, Su D et al (2024) Constructing fully-active and ultra-active sites in high-entropy alloy nanoclusters for hydrazine oxidation-assisted electrolytic hydrogen production[J]. Adv Mater 36(13):2309715. https://doi.org/10.1002/adma.202309715
77. Rittiruam M, Khamloet P, Tantitumrongwut P et al (2023) First-principles active-site model design for high-entropy-alloy catalyst screening: the impact of host element selection on catalytic properties[J]. Adv Theory Simul 6(11):2300327. https://doi.org/10.1002/adts.202300327
78. Ming S, Meng K, Hou C et al (2023) Electron-level insight into efficient synergistic oxygen evolution catalysis at multimetallic sites in PtNiFeCoCu high-entropy alloys[J]. Phys Chem Chem Phys 25(48):32979–32988. https://doi.org/10.1039/d3cp04829b